Supporting Information

Optimized Fibril Morphology of Polymer Donor by Increasing Dipole-Dipole Interaction via Additive Toward Efficient Organic Solar Cells

Yu Shen[a, b], Hanyue Gao [a, b], Ziwen Yu[c], Mingyu Zuo[a, b], Luzhuo Li[a, b], Sichao Huang[a, b], Zhongxiang Peng[a], Qing Jiang[c], Tonghui Wang[c], Qiang Zhang[*a], Rui Zhang[*d], Yanchun Han[*a, b]

[a] State Key Laboratory of Polymer Science and Technology, Changchun Institute of Applied Chemistry, Chinese Academy of Sciences, Changchun 130022, P. R. China

[b] School of Applied Chemistry and Engineering, University of Science and Technology of China, Hefei 230026, P. R. China

[c] Key Laboratory of Automobile Materials, Ministry of Education, School of Materials Science and Engineering, Jilin University, Changchun 130022, China

[d] State Key Laboratory of Bioinspired Interfacial Materials Science, Institute of Functional Nano & Soft Materials (FUNSOM), Soochow University, Suzhou 215123, P. R. China

*** Corresponding authors:**

E-mail:

Qiang Zhang

zhqawh@ciac.ac.cn

Rui Zhang

rui.zhang@suda.edu.cn

Yanchun Han

ychan@ciac.ac.cn

1. Experimental Methodology

Materials

Poly[(2,6-(4,8-bis(5-(2-ethylhexyl-3-fluoro)thiophen-2-yl)-benzo[1,2-b:4,5-b']dithiophene))-alt-5,5'-(5,8-bis(4-(2-butyloctyl)thiophen-2-yl)dithieno[3',2':3,4;2'',3'':5,6]benzo[1,2-c][1,2,5]thiadiazole)] (D18) (Mw=97kDa, PDI=2.09), 2,2′-((2Z,2′Z)-((3,9-bis(2-butyloctyl)−12,13-bis(2-ethylhexyl)−12,13 dihydro[1,2,5]thiadiazolo[3,4e]thieno[2″,3″:4′,5′]thieno[2′,3′:4,5]pyrrolo[3,2 g]thieno[2′,3′:4,5]thieno[3,2b]indole-2,10-diyl)-bis-(methaneylylidene))-bis-(5,6-difluoro-3-oxo-2,3-dihydro-1Hindene-2,1-diylidene))dimalononitrile (L8-BO) were purchased from Organtec Ltd. 2, 4-dichloro-5-cyanothiazole (DCCTz) was purchased from Macklin. Poly(3,4-ethylenedioxythiophene):polystyrene sulfonate (PEDOT:PSS, Clevios AI 4083) was purchased from Heraeus. poly[(9,9-bis(3’-(N,N-dimethylamino)propyl)-2,7-fluorene)-alt-5,5’-bis(2,2’-thiophene)-2,6-naphthalene-1,4,5,8-tetracaboxylic-N,N’-di(2-ethylhexyl)imide](PNDIT-F3N) was purchased from Volt-Amp Ltd. Chloroform (CF), toluene, acetone and ethanol were purchased from Xilong Scientific Co., Ltd. Methanol was purchased from Sigma-Aldrich. All the chemicals were used as received and without any treatment.

OSCs Device fabrication

All the organic solar cells were fabricated with a structure of indium tin oxide (ITO)/PEDOT:PSS/active layer/PNDIT-F3N/Ag. The patterned ITO glass substrate was pre-cleaned by toluene, acetone, ethanol and deionized water in an ultrasonic bath for 20 min successively and finally dried with high purity nitrogen. The pre-cleaned ITO substrate was treated by ultraviolet ozone for 20 min firstly. PEDOT:PSS was spin-coated on the treated ITO substrate at a spin speed of 6000rpm for 20 s, and then baked on a hotplate at a temperature of 150 °C for 15 min. The optimized thickness of PEDOT:PSS layer is about 20 nm. Then the substrates were transferred to a nitrogen-filled glove box for further casting processes. The active layer was casted by layer-by-layer spin coating strategy. D18 was dissolved in CF at a concentration of 5 mg mL^{-1} (without or with 25, 50, 75, 100 wt% DCCTz) at 75 °C for 1 h and spin coated on PEDOT:PSS layer at 3300 rpm for 30 s, with a thickness of ~50 nm. After thermal annealing at 90 °C for 5 min, L8-BO solution which dissolved in CF at a concentration of 8 mg mL^{-1} was spin coated on D18 layer at 3500 rpm for 30 s, with a total thickness of ~100 nm. Then the whole substrates were thermal annealed at 90 °C for 5 min. After that, a solution of 1 mg mL^{-1} PNDIT-F3N dissolved in methanol (with 1 vol% acetic acid) was spin-coated onto the active layer at 3000 rpm for 20 s. Finally, a 150 nm Ag layer was deposited at vacuum of lower than 1×10^{-4} kPa. The effect area of the device was standardized by a 0.04 cm^2 mask.

Device characterization and EQE measurements

The J-V curves were performed by Keithley 2400 light source meter under AM 1.5G illumination (100 mW cm^{-2}) using a solar simulator. The test was conducted in a nitrogen-filled glove box, and the test bias voltage range was from -0.5 V to 1.2 V. The external quantum efficiency (EQE) measurement was obtained in air atmosphere using the QE-R 3011 solar cell quantum efficiency testing system from Enli Tech. The light intensity at each tested wavelength (300-1000 nm) was calibrated using a standard Si photovoltaic cell.

Space-charge-limited current (SCLC) measurement

The hole-only devices were fabricated with a structure of ITO/PEDOT:PSS/D18 or Active layer/MnO_3/Ag. The electron-only devices were fabricated with a structure of ITO/ZnO/Active layer/PNDIT-F3N/Ag. The D18 layer or D18/L8-BO layer were prepared under the same conditions as device fabrication process and being thermal annealed. All the carrier mobility were obtained by SCLC method according to the formula $J=\frac{9}{8}\varepsilon_0\varepsilon_r\mu\frac{V^2}{d^3}$, where J is the current density, ε_0 is the permittivity in free space (8.85×10^{-14} F cm^{-1}), ε_r is the relative dielectric constant of the organic active layer (3.00), μ is the carrier mobility, V is the effective voltage and d is the thickness of the active layer.

OFET devices fabrication and measurements

The OFET devices were fabricated in bottom gate, top contact structure. The pre-cleaned 1.5×1.5 cm Si/SiO_2 substrate was treated by UV/Ozone for 25 min. Then the OTCS solution (1.3 μL mL^{-1}) was casted on the substrate and let stand for 10 s, followed by spin coating at 3000 rpm for 30s. Subsequently, the substrates were exposed to ammonia atmosphere for 8 h, followed by cleaning with toluene and isopropanol for use. D18 solution (prepared as OSCs device fabrication) was spin coated on the treated substrates at 3000 rpm for 30 s and then treated with thermal annealing at 90 °C for 5 min. Finally, gold was deposited under high vacuum conditions as the source and drain electrodes.

The OFET devices were tested in an air environment by a probe station connected to a Keysight B1500A semiconductor parameter analyzer, where the transfer curves were obtained. The carrier mobility (μ_{sat}) was calculated from the transfer curve from the following equation: $\mu_{sat} = \left(\frac{\partial\sqrt{I_D}}{\partial V_G}\right)^2 (2L / WC_i)$, where e μ_{sat} is the carrier mobility, I_D is the drain-source current, V_G is the gate voltage, C_i (5 nF cm^{-2}) is the capacitance per unit area of the dielectric in OFET device.

Ultraviolet-visible (UV-vis) absorption spectra

The ultraviolet-visible (UV-vis) absorption spectra were collected at a wavelength range of 400-1000 nm by a Lambda 750 spectrometer (Perkin-Elmer, Wellesley, MA). For film measurement, 5 mg mL^{-1} D18 solution without/with 25 wt%, 50 wt% 75 wt% and 100 wt% DCCTz was spin coated on a glass substrate under the same conditions as device fabrication process and being thermal annealed. For solution measurement, 20 μL D18 solution at 5 mg/mL without/with 25 wt%, 50 wt% 75 wt% and 100 wt% DCCTz was dropped between two glass sheets and then be tested immediately.

Fourier transform infrared spectrometer (FT-IR) spectra

The FT-IR spectra were measured by a Bruker VERTEX 70 V FT-IR spectrometer using KBr pellets as substrates, where all the solution was drop-coated onto the pellet and being tested after the solution was totally dried in air, except for the thermal annealed sample. The D18 solution was 5 mg mL^{-1} with or without 50 wt% DCCTz and the DCCTz solution was 50 mg mL^{-1}. The thermal annealing condition was 5 min at 90 °C. The data were analyzed using OPUS software. The test range was 4000-400 cm^{-1}.

Thermogravimetric (TGA) measurement

The TGA was conducted by Thermo Plus EVO (Rigaku Corporation) at a N_2 atmosphere with a heating rate of 5 °C min^{-1} from 25 °C to 200 °C, with a N_2 rate of 90 mL min^{-1}. The tested DCCTz sample was 15 mg.

Atomic force microscopy (AFM)

The AFM images were tested with a from SPA-300HV (Seiko Instruments Inc., Japan) in tapping mode. The probe used was a Si cantilever with a force constant of 2 N m^{-1} and a resonance frequency of 70 kHz. The film samples were spin-cast onto PEDOT:PSS-coated glass substrates using the same conditions as device preparation and being thermal annealed at 90 °C 5 min. The row data and 1D line cut profile data was obtained and treated by Gwyddion software. The fiber width is obtained by analyzing the FWHM in the line cut profile curves and being counted by OriginPro 2025b software. The fiber length data was fitted by GTFiber software. In the GTFiber analysis, AFM images were first processed by noise filtering and adaptive thresholding to distinguish fibrillar structures from the background. The identified fibrils were then skeletonized into one-pixel-wide backbones, from which the fibril length was calculated based on the connected path of each fibril. This approach enables statistical extraction of fibril length distributions from a large number of individual fibrils within a single image.

Transmission electron microscopy (TEM)

The TEM images were obtained by a JEOL JEM-1011 transmission electron microscope operated at an acceleration voltage of 100 kV. The samples were spin-coated on a PEDOT:PSS-coated glass substrate following 90 °C thermal annealing and then dissolved PEDOT:PSS in deionized water to make the sample film float on the surface of water[1]. Next, we used copper grids to collect the sample films and dried in a vacuum chamber overnight.

Grazing incidence wide-angle X-ray scattering (GIWAXS)

The GIWAXS data were obtained at Shanghai Synchrotron Radiation Facility (SSRF) of BL16B1 beamline. The samples were prepared on Si substrates with a PEDOT:PSS coated layer using the same condition as device fabrication. The wavelength (λ) of monochromatic X-ray beam was 1.24 Å with an energy of 10 keV.

The incidence angle was 0.15 °, along with an exposure time of 30 s. The 2D GIWAXS patterns were collected by Pliatus 900K at a distance placed 245 mm downstream. The 1D profiles and azimuthal integration analysis data were obtained with GIWAXS-Tool software (Ver. 2. 18. 11).

In-situ UV-vis absorption spectra

The in-situ UV-vis spectra during the spin-coating process were measured using spectrometer (DU100, Shaanxi Puguang Weishi Co. Ltd.) with a scan range of 400-1000 nm. The sampling interval was 5 ms with an integration time of 20 ms per sample point. The spin coating process is controlled as the same as device fabrication.

The in-situ UV-vis spectra during thermal annealing process were measured using Lambda 750 spectrometer (Perkin-Elmer, Wellesley, MA) with a scan range of 400-1000 nm. The samples were prepared by spin coating 5 mg mL^{-1} D18 solution without/with 25 wt%, 50 wt% 75 wt% and 100 wt% DCCTz on a glass substrate under the same conditions as device fabrication process but without thermal annealing. The sample was placed on a hot plate of 90 °C. The time delay between scans was 1 s, with an integration time of 100 ms for each point.

Cross-sectional scanning electron microscopy

The cross-sectional SEM were obtained by a Hitachi SU8600 scanning electron microscope. The samples were prepared on Si substrates using the same condition as device fabrication and being thermal annealed. Then the film was immersed in liquid nitrogen for 1 minute, and then it was broken immediately to expose the cross-section for SEM testing.

2. Computational Methodology

Electrostatic potential (ESP) and independent gradient model based on Hirshfeld partitioning (IGMH) analysis

The ESP calculations were experimented by density functional theory (DFT) method with the ORCA 5.0.4 software package[1]. The geometry optimization and single point energy were calculated at the B3LYP/def2-SVP level with d3 dispersion correction. The wave function results were further analyzed by Multiwfn 3.8 software[2]. The ESP distributions and IGMH iso surfaces were visualized by VMD 1.9.3 software[3].

Molecular dynamics (MD) simulations

The MD simulations were performed with the LAMMPS package[4] and the force field of optimized potentials for liquid simulations - all atom (OPLS-AA)[5-8]. To accurately capture the intramolecular and intermolecular interactions for D18 and DCCTz, the force field was reparametrized according to the long-range corrected DFT calculations: (i) the atomic partial charges were derived by fitting the electrostatic potential (ESP) from DFT calculations at the ωB97XD/cc-PVTZ level of theory; (ii) the bond lengths and angles were taken from the geometries optimized at the ωB97XD/6-31G(d,p) level of theory, with the harmonic force constants kept as they are; and (iii) the parameters for the inter-ring dihedrals along the D18 chain were fitted on the basis of their torsion potentials evaluated at the ωB97XD/6-31G(d,p) level of theory. Here, the relevant DFT calculations were performed with the Gaussian 16 C.01 package[9], and the ω range-separation parameters were optimized in gas phase.

The initial models for neat D18 film and D18 film with DCCTz additive were built by randomly placing 40 D18 chains (each chain has 6 repeat units) and 40 D18 chains with 912 DCCTz molecules in two cubic cells with a low density of 0.02 g cm^{-3}, respectively. Here, the choices of D18 chain length, and numbers of D18 chains and DCCTz molecules were based on two considerations, *i.e.*, the 2:1 weight ratio between D18 and DCCTz in experiment, and the computational feasibility. The MD simulations were first run with the NPT (constant number of molecules, pressure, and temperature) ensembles for 30 ns at a temperature of 600 K and a pressure of 1 atm. Then, the two films were rapidly cooled from 600 K to 363.15 K, with a cooling rate of ~50 K ns^{-1}. To simulate to the experimental annealing process, the MD simulations were finally carried out (i) at 363.15 K for 20 ns; (ii) from 363.15 K to 298.15 K with a slow cooling rate of ~2 K ns^{-1}; (iii) at 298.15 K for 10 ns, where 363.15 K was the experimental annealing temperature. A cutoff of 12 Å was used for the summation of the van der Waals interactions and the particle-particle particle-mesh (PPPM) solver for the long-range Coulomb interactions. The Verlet integrator was used with a timestep of 1 fs and the Nosé-Hoover thermostat / barostat was employed for temperature / pressure control.

Intermolecular interaction calculations

The intermolecular backbone-backbone interaction energies for D18_D18 π-π packing pairs were calculated at the ωB97XD/6-31G(d,p) level of theory, where all pair geometries were kept as those extracted from the MD-simulated films and all side chains were replaced with methyl groups. To avoid the overstabilization of these energies induced by basis set superposition error, we employed the counterpoise correction method proposed by Boys and Bernardi[10].

Hole transfer rate calculations

The semi-classical Marcus theory was used to evaluate the hole transfer rate, k_h, between two D18 chains in a π-π packing pair[11]:

$$k_h = \frac{2\pi}{\hbar}\frac{|V_i|^2}{\sqrt{4\pi\lambda_i k_\mathrm{B}T}}exp[-\frac{(\Delta E_i + \lambda)^2}{4\lambda_i k_\mathrm{B}T}]$$

where $\hbar$ represents the reduced Planck's constant; V_i, the electronic coupling between the initial and final states; λ_i, the reorganization energy; k_B, the Boltzmann constant; T, the temperature (298.15 K); and ΔE_i, the energy difference between the initial and final states. V_i or ΔE_i between the initial and final states was approximated as that between the highest occupied molecular orbitals of two D18 chains in the π-π packing pair; V_i was examined by the fragment orbital method[12]. The λ_i reorganization energy consists of intra- (λ_{intra}) and intermolecular (λ_{inter}) contributions. The former was evaluated from the adiabatic potential energy surfaces of the molecular states involved in the charge transfer process, while the latter was set to 0.1 eV (a reasonable value for extended π-conjugated systems)[13, 14], considering that there are currently no straightforward models to accurately estimate the λ_{inter} value in solid-state environments. Here, the DFT calculations were performed at the PCM-tuned-ωB97XD/6-31G(d,p) level of theory ("PCM-tuned" means that the ω range-separation parameter was optimized with the polarizable continuum model and a typical dielectric constant of 3.5)[15, 16].

3. Supporting Figures

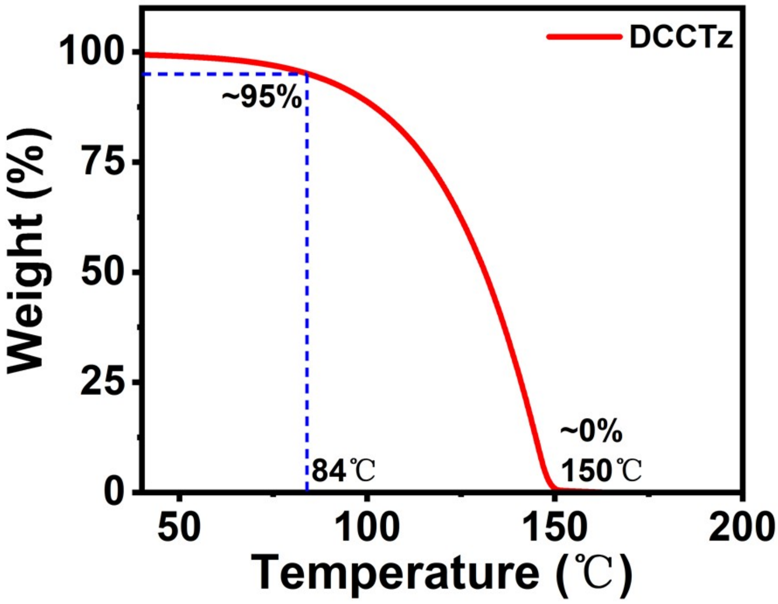

Figure S1. TGA curves of DCCTz.

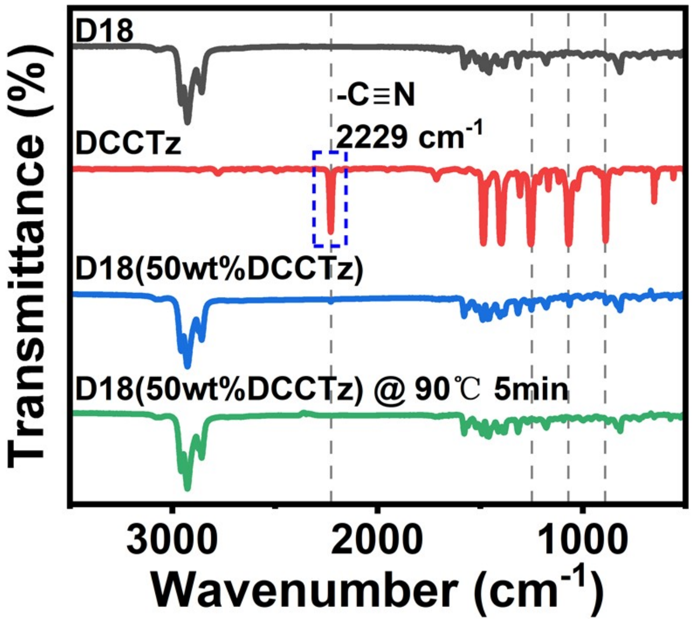

Figure S2. FT-IR spectra of pristine D18, DCCTz and D18 films treated with DCCTz before and after thermal annealing.

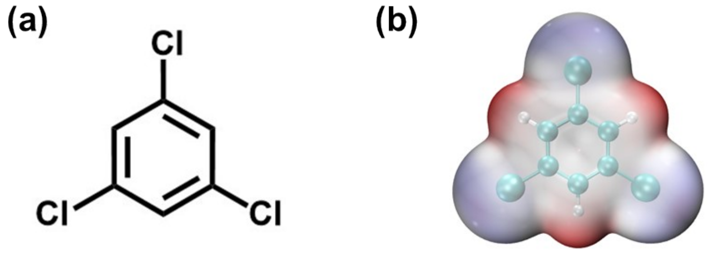

Figure S3. (a) The chemical structure of TCB. (b) The ESP distrbution of TCB

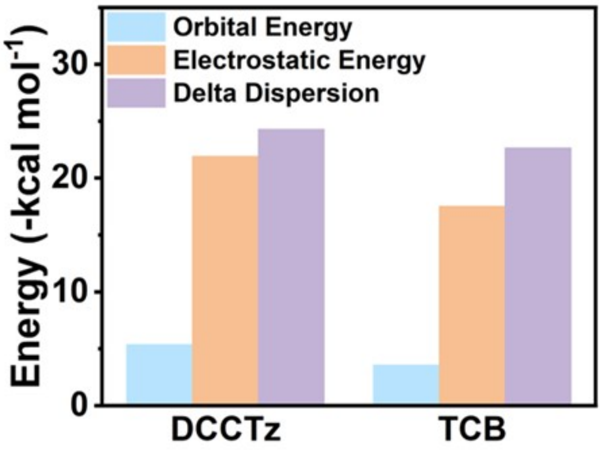

Figure S4. EDA results of the interaction of D18 with DCCTz and TCB.

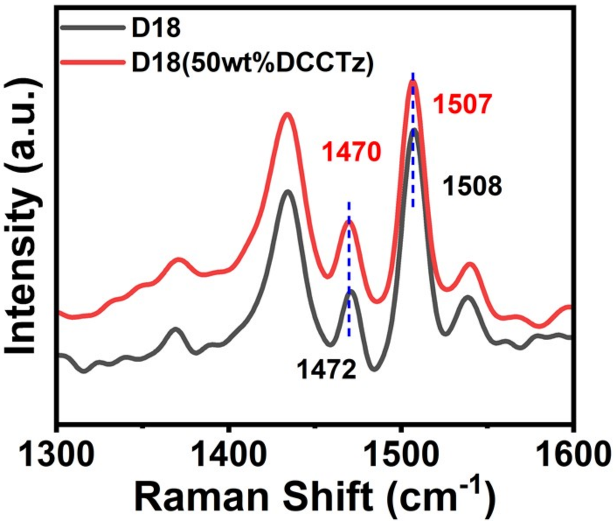

Figure S5. Raman spectra of the aromatic ring skeleton vibration band in D18.

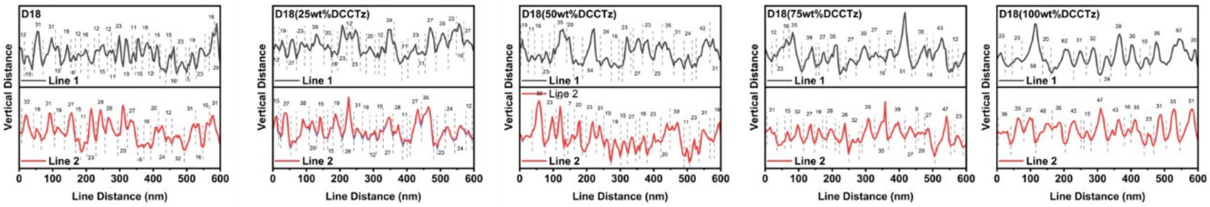

Figure S6. Line profiles of D18 films to obtain the fibril width from the full width at half maximum (FWHM).

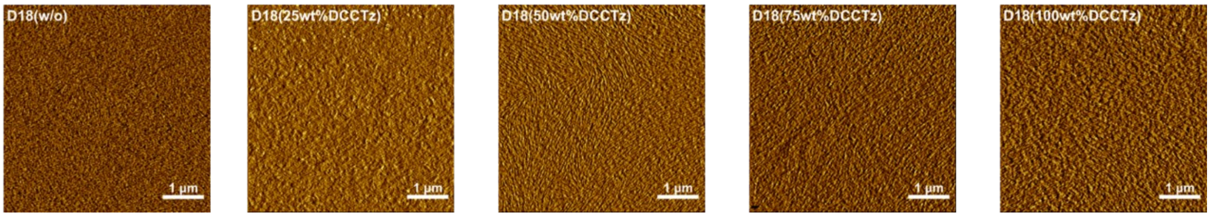

Figure S7. 5×5μm^2 AFM phase images of D18 films.

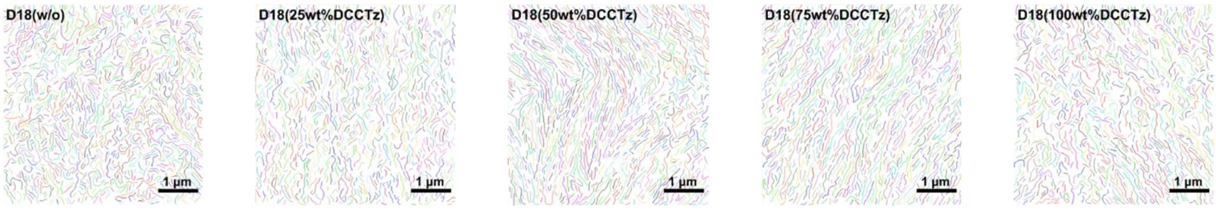

Figure S8. Fiber length mapping extracted from 5*5 μm^2 AFM phase images using GTFiber software.

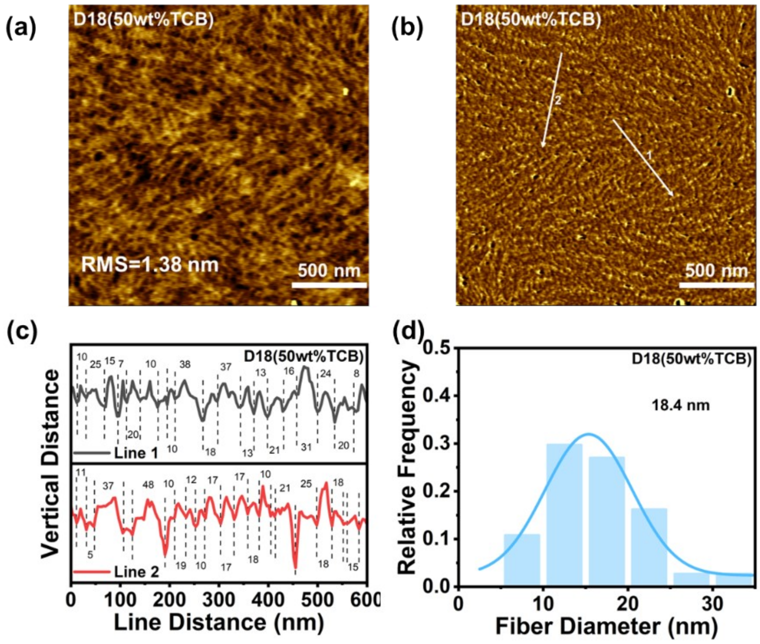

Figure S9. (a) Height images of D18 film treated with TCB. (b) Phase images of D18 film treated with TCB. (c) Line profiles of D18 film treated with TCB to obtain the fibril width from the FWHM. (d) Statistical results.

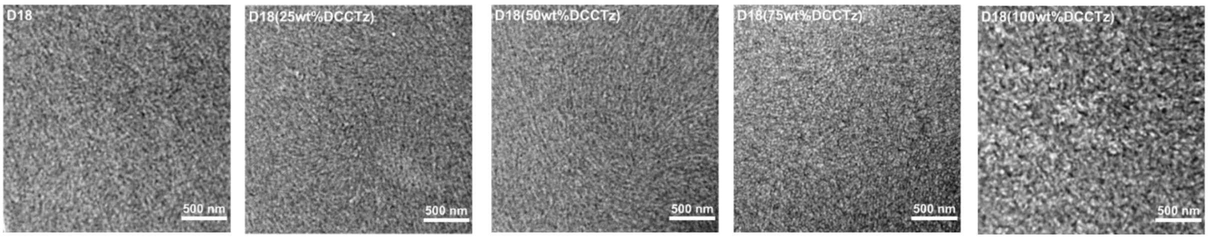

Figure S10. TEM images of D18 films treated without or with 25, 50, 75 and 100 wt% DCCTz content.

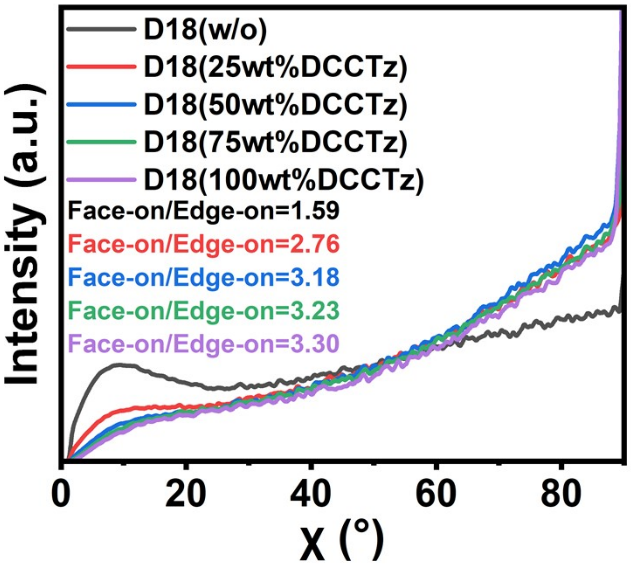

Figure S11. The azimuthal curves of D18 films treated without or with 25, 50, 75 and 100 wt% DCCTz content.

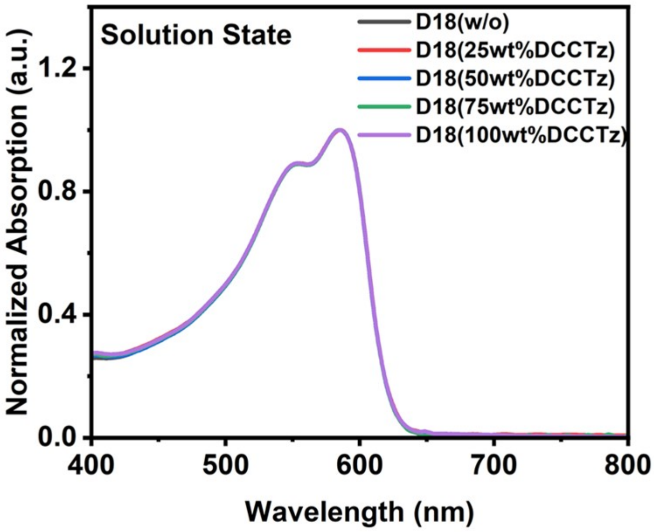

Figure S12. UV-vis absorption spectra of D18 solutions treated with various contents of DCCTz.

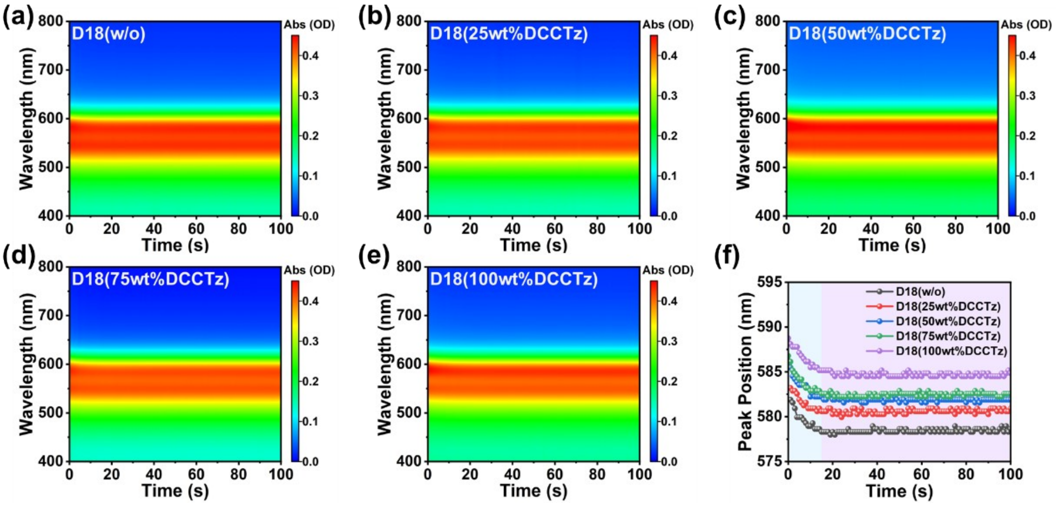

Figure S13. (a-e) The in-situ absorption speactra of D18 films treated without or with 25, 50, 75, 100 wt% DCCTz content during thermal annealing process. (f) The 0-0 peak position changes extracted from in-situ absorption speactra during thermal annealing process.

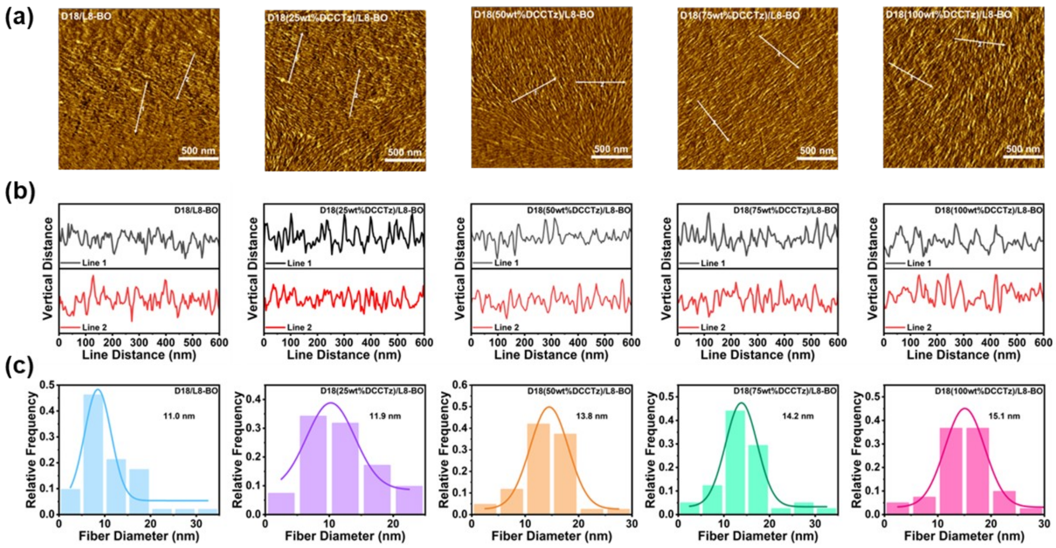

Figure S14. (a) Phase images of D18/L8-BO layer-by-layer film. (b) Line profiles of D18/L8-BO films to obtain the fibril width from the FWHM. (c) Statistical results.

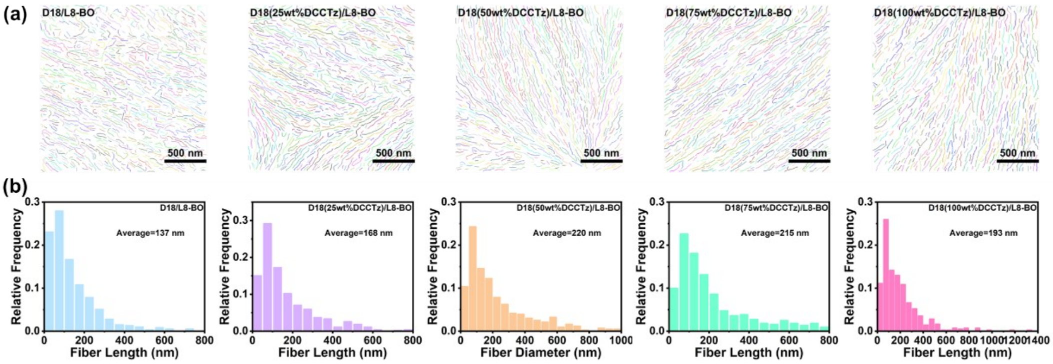

Figure S15. (a) Fitting diagram results of fiber length treated by GTFiber software. (b) Statistical results.

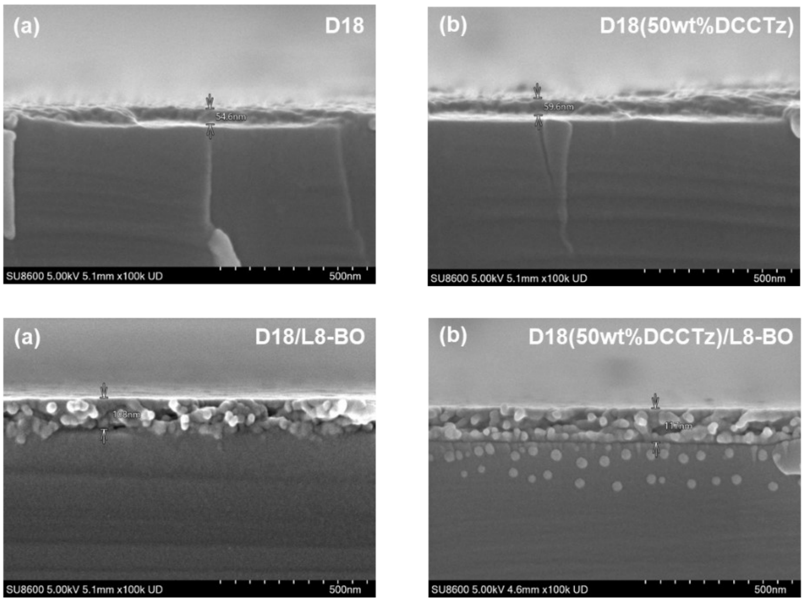

Figure S16. Cross-sectional SEM of (a-b) D18 films and (c-d) D18/L8-BO LBL films.

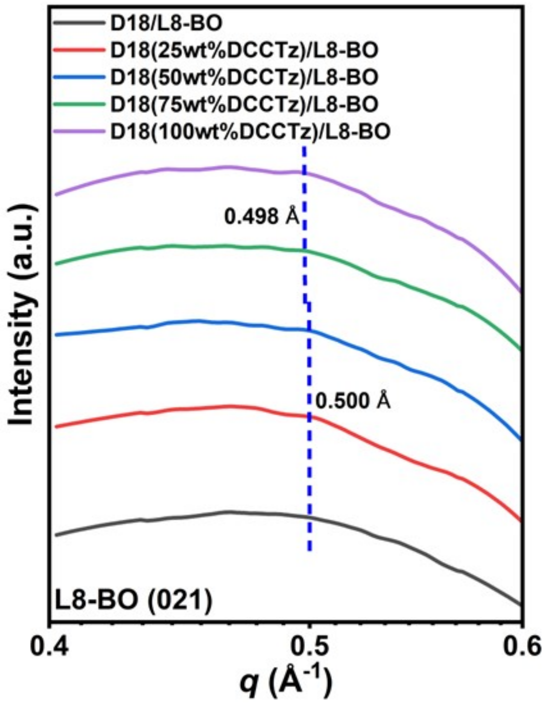

Figure S17. The integrate curve of D18/L8-BO films from an azimuthal angle from 20° to 70°.

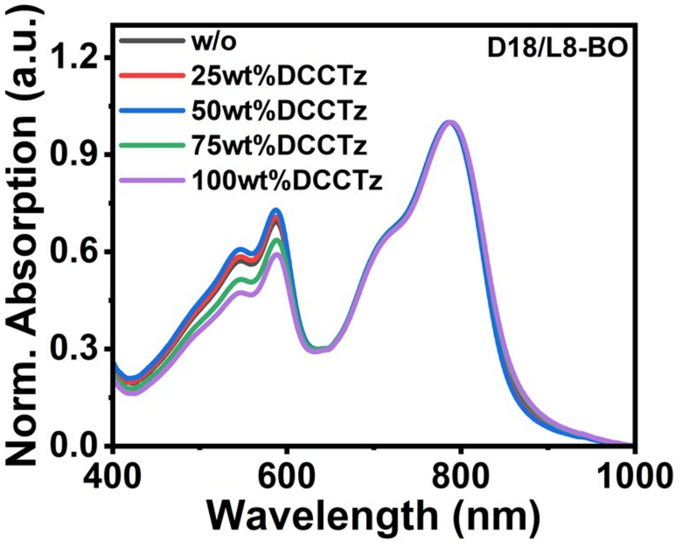

Figure S18. UV-vis spectra of D18/L8-BO films.

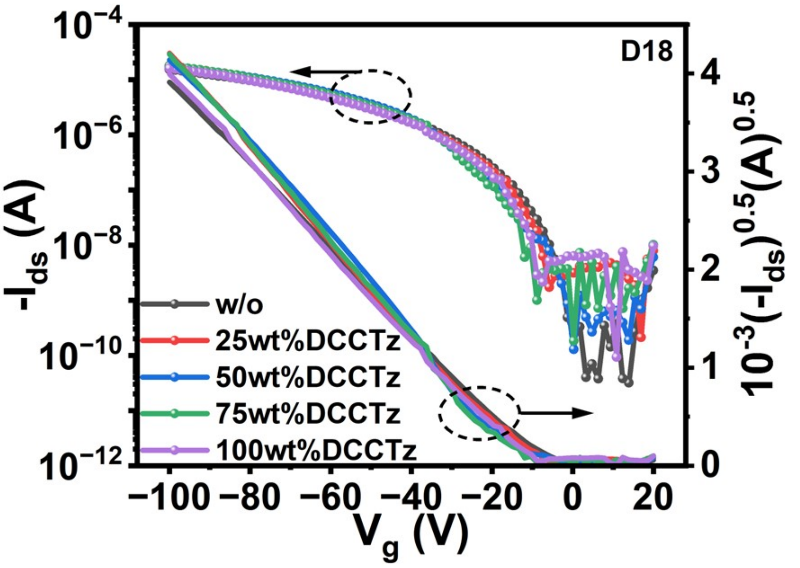

Figure S19. Typical transfer characteristics of OFET based on D18 films treated without or with 25, 50, 75, 100 wt% DCCTz.

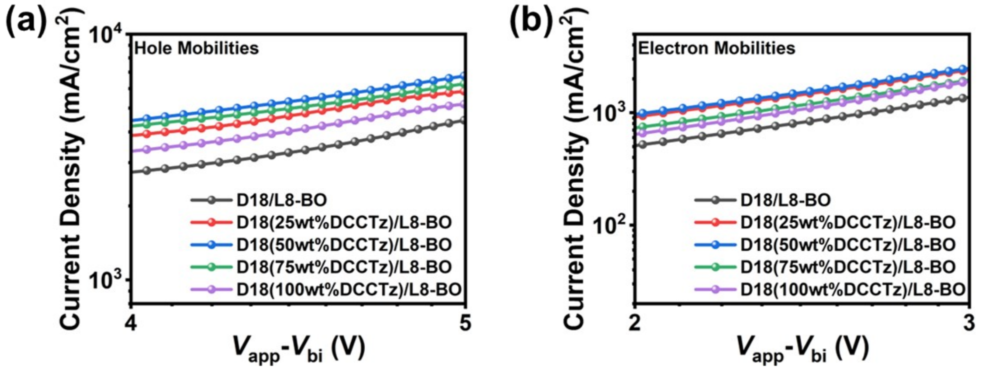

Figure S20. *J*-*V* curves of SCLC test at dark state. (a) Hole mobility of D18/L8-BO active layer processed without and with DCCTz. (b) Electron mobility of D18/L8-BO active layer processed without and with DCCTz.

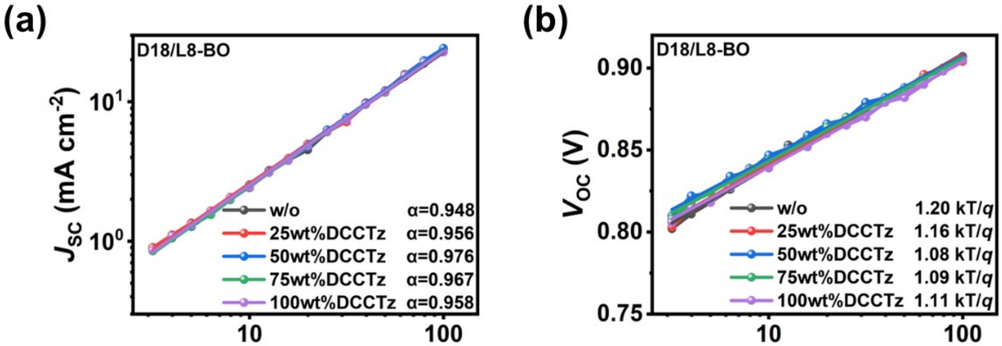

Figure S21. The light intensity dependence curves of (a) J_{SC} and (b) V_{OC}.

4. Supporting Tables

Table S1. Detalied EDA results of the interaction of D18 with DCCTz and TCB.

	Orbital Energy (kcal mol^{-1})	Electrostatic Energy (kcal mol^{-1})	Delta Dispersion (kcal mol^{-1})
DCCTz	-5.36	-21.92	-24.30
TCB	-3.57	-17.53	-22.66

Table S2. Peak analysis results of the normalized UV-vis absorption spectra.

DCCTz content	0-0 Peak position (nm)	0-1 Peak position (nm)	I_{0-0}/I_{0-1}
w/o	584	547	1.08
25wt%	584	548	1.08
50wt%	585	547	1.10
75wt%	586	547	1.10
100wt%	587	548	1.11

Table S3. Summary statistics of fibril lengths in D18 films extracted from AFM images of thin films prepared at different additive contents.

DCCTz content	Number of fibrils	Average length (nm)	Medium length (nm)	Q1 (nm)	Q3 (nm)
w/o	809	264	190	122	333
25wt%	632	313	215	131	387
50wt%	644	390	270	145	503
75wt%	610	381	265	146	472
100wt%	652	302	215	130	383

Table S4. Parameters of D18 films treated by various DCCTz contents revealed by GIWAXS measurement.

Peak	Content	w/o	25wt%	50wt%	75wt%	100wt%
OOP (100)	q ($Å^{-1}$)	0.295	0.275	0.268	0.268	0.265
	d-spacing (Å)	21.3	22.8	23.4	23.4	24.2
	FWHM ($Å^{-1}$)	0.08	0.09	0.09	0.09	0.09
	CCL (Å)	69.9	62.13	62.13	62.13	62.13
OOP (010)	q ($Å^{-1}$)	1.697	1.697	1.703	1.705	1.705
	d-spacing (Å)	3.70	3.70	3.69	3.68	3.68
	FWHM ($Å^{-1}$)	0.22	0.20	0.19	0.19	0.18
	CCL (Å)	25.4	28.0	29.4	29.4	31.1
IP (100)	q ($Å^{-1}$)	0.310	0.310	0.310	0.310	0.310
	d-spacing (Å)	20.3	20.3	20.3	20.3	20.3
	FWHM ($Å^{-1}$)	0.08	0.09	0.09	0.09	0.09
	CCL (Å)	75.8	101.7	109.6	107.5	105.5

Table S5. Face-on/edge-on result extracted from the azimuthal integral curves of D18 films treated with various DCCTz contents.

Content	Face-on/edge-on
w/o	0.42
25wt%	0.90
50wt%	1.19
75wt%	1.24
100wt%	1.32

Table S6. The inter-chain interaction energy calculation results of the D18 molecules before and after the addition of DCCTz.

System	D18-A_D18-A (kcal mol^{-1})	D18-D_D18-A (kcal mol^{-1})	D18-D_D18-D (kcal mol^{-1})	Average (kcal mol^{-1})
w/o	-20.7	-19.7	-20.8	-20.1
50wt% DCCTz	-22.8	-20.1	-21.2	-21.9
difference	2.11	0.43	0.40	1.78

Table S7. Detailed statistics of A_A, A_D and D_D ratios in π-π stacking patterns.

System	Packing pattern	Proportion	
		number	π-π ratio
w/o	D18-A_D18-A	41 (62.12%)	66 (29.07%)
	D18-D_D18-A	23 (34.85)	
	D18-D_D18-D	2 (3.03%)	
50wt% DCCTz	D18-A_D18-A	37 (54.41%)	68 (20.67%)
	D18-D_D18-A	26 (38.24%)	
	D18-D_D18-D	5 (7.35%)	

Table S8. Summary statistics of fibril lengths in D18/L8-BO films extracted from AFM images of thin films prepared at different additive contents.

DCCTz content	Number of fibrils	Average length (nm)	Medium length (nm)	Q1 (nm)	Q3 (nm)
w/o	612	137	95	52	184
25wt%	539	168	116	62	220
50wt%	433	220	153	73	293
75wt%	442	216	148	79	277
100wt%	424	193	146	67	250

Table S9. Parameters of D18/L8-BO films treated various DCCTz contents revealed by GIWAXS measurement.

Peak	Content	w/o	25wt%	50wt%	75wt%	100wt%
OOP (100)	q ($Å^{-1}$)	0.282	0.280	0.275	0.275	0.275
	d-spacing (Å)	22.28	22.44	22.85	22.85	22.85
	FWHM ($Å^{-1}$)	0.09	0.09	0.09	0.09	0.10
	coherence length (Å)	62.13	62.13	62.13	62.13	55.92
OOP (010)	q ($Å^{-1}$)	1.708	1.723	1.725	1.725	1.725
	d-spacing (Å)	3.68	3.65	3.64	3.64	3.64
	FWHM ($Å^{-1}$)	0.27	0.25	0.25	0.25	0.25
	CCL (Å)	20.71	22.37	22.37	22.37	22.37
IP (100)	q ($Å^{-1}$)	0.315	0.313	0.313	0.313	0.315
	d-spacing (Å)	19.95	20.07	20.07	20.07	19.95
	FWHM ($Å^{-1}$)	0.08	0.08	0.08	0.08	0.08
	CCL (Å)	69.90	69.90	69.90	69.90	69.90
L8-BO (021)	q (Å-1)	0.500	0.500	0.500	0.498	0.498
	d-spacing (Å)	12.57	12.57	12.57	12.62	12.62
	FWHM ($Å^{-1}$)	0.13	0.13	0.13	0.14	0.14
	CCL (Å)	43.02	43.02	43.02	39.94	39.94

Table S10. Detailed photovoltaic parameters of device based on D18(50wt% DCCTz)/L8-BO.

	V_{OC} (V)	J_{SC} (mA cm^{-2})	FF (%)	PCE (%)
1	0.905	26.36	80.88	19.30
2	0.910	26.46	79.99	19.27
3	0.906	26.27	80.61	19.19
4	0.908	26.22	80.55	19.18
5	0.905	26.31	80.21	19.11
6	0.903	26.37	80.24	19.11
7	0.904	26.23	80.22	19.03
8	0.904	26.11	80.29	18.95
9	0.903	26.15	80.20	18.95
10	0.904	26.16	80.04	18.93

Table S11. Photovoltaic parameters of the OSCs based on D18/L8-BO (w/o) with thermal annealing for 5 minutes at different temperatures.

TA Temperature (°C)	V_{OC} (V)	J_{SC} (mA cm^{-2})	FF (%)	PCE (%)
70	0.921	25.07	75.49	17.45
	(0.920±0.002)	(24.97±0.21)	(75.22±0.52)	(17.28±0.25)
80	0.914	25.75	75.18	17.70
	(0.920±0.002)	(25.56±0.41)	(74.68±0.46)	(17.47±0.23)
90	0.918	25.79	75.72	17.93
	(0.916±0.003)	(25.59±0.33)	(74.84±0.76)	(17.55±0.19)
100	0.911	25.90	74.89	17.67
	(0.910±0.003)	(25.78±0.15)	(74.51±0.83)	(17.48±0.22)

Table S12. The hole transport coupling results of the D18 molecules before and after the addition of DCCTz.

System	λ (meV)	ΔE_{ij} (avg.) (meV)		V (avg.) (meV)	k_e (avg.) (s^{-1})	
D18(50wt%DCCTz)	438.5	-99.63	99.63	9.39	1.41×10^{12}	2.28×10^{10}
D18	438.5	-99.31	99.31	7.76	1.10×10^{12}	1.02×10^{10}

Table S13. The statistical results of hole transfer rates in different magnitudes.

hole-transfer rate [s^{-1}]	D18	D18(50wt% DCCTz)
$\geq10^{13}$	2.94%	3.03%
$\geq10^{12}$	11.76%	12.12%
$\geq10^{11}$	27.94%	34.85%
$\geq10^{10}$	51.47%	59.09%

Table S14. The hole mobilty of D18 films tested by fabricated OFET devices.

System	**μ_h (10^{-2} cm^2 V^{-1} s^{-1})**
D18	7.57
D18(25wt%DCCTz)	8.99
D18(50wt%DCCTz)	10.10
D18(75wt%DCCTz)	9.72
D18(100wt%DCCTz)	8.00

Table S15. Charge mobility parameters of the D18 monolayer and D18/L8-BO devices extracted from SCLC method.

Systems	μ_h **(10^{-4} cm^2 V^{-1} s^{-1})**	μ_e **(10^{-4} cm^2 V^{-1} s^{-1})**	μ_e/μ_h
D18/L8-BO	2.66	4.02	1.51
D18 (25wt%DCCTz)/L8-BO	5.95	6.99	1.17
D18 (50wt%DCCTz)/L8-BO	7.84	7.49	0.95
D18 (75wt%DCCTz)/L8-BO	7.32	6.37	0.87
D18 (100wt%DCCTz)/L8-BO	5.06	4.31	0.85

5. References

1. S. Rechberger, N. Gasparini, R. Singh, M. Kim, C. L. Chochos, V. G. Gregoriou, K. Cho, C. J. Brabec, T. Ameri and E. Spiecker, Sol. RRL, 2020, 4, 8.
2. F. Neese, WIREs Computational Molecular Science, 2022, 12, e1606.
3. T. Lu and F. Chen, Journal of Computational Chemistry, 2012, 33, 580-592.
4. W. Humphrey, A. Dalke and K. Schulten, Journal of molecular graphics, 1996, 14, 33-38.
5. S. Plimpton, Journal of computational physics, 1995, 117, 1-19.
6. T. Wang, M. K. Ravva and J. L. Brédas, Advanced Functional Materials, 2016, 26, 5913-5921.
7. T. Wang and J.-L. Bredas, Matter, 2020, 2, 119-135.
8. W. L. Jorgensen and J. Tirado-Rives, Journal of the American Chemical Society, 1988, 110, 1657-1666.
9. N. E. Jackson, K. L. Kohlstedt, B. M. Savoie, M. Olvera de la Cruz, G. C. Schatz, L. X. Chen and M. A. Ratner, Journal of the American Chemical Society, 2015, 137, 6254-6262.
10. M. J. Frisch, G. W. Trucks, H. B. Schlegel, G. E. Scuseria, M. A. Robb, J. R. Cheeseman, G. Scalmani, V. Barone, G. A. Petersson, H. Nakatsuji, X. Li, M. Caricato, A. V. Marenich, J. Bloino, B. G. Janesko, R. Gomperts, B. Mennucci, H. P. Hratchian, J. V. Ortiz, A. F. Izmaylov, J. L. Sonnenberg, Williams, F. Ding, F. Lipparini, F. Egidi, J. Goings, B. Peng, A. Petrone, T. Henderson, D. Ranasinghe, V. G. Zakrzewski, J. Gao, N. Rega, G. Zheng, W. Liang, M. Hada, M. Ehara, K. Toyota, R. Fukuda, J. Hasegawa, M. Ishida, T. Nakajima, Y. Honda, O. Kitao, H. Nakai, T. Vreven, K. Throssell, J. A. Montgomery Jr., J. E. Peralta, F. Ogliaro, M. J. Bearpark, J. J. Heyd, E. N. Brothers, K. N. Kudin, V. N. Staroverov, T. A. Keith, R. Kobayashi, J. Normand, K. Raghavachari, A. P. Rendell, J. C. Burant, S. S. Iyengar, J. Tomasi, M. Cossi, J. M. Millam, M. Klene, C. Adamo, R. Cammi, J. W. Ochterski, R. L. Martin, K. Morokuma, O. Farkas, J. B. Foresman and D. J. Fox, 2016, Gaussian 16 Rev. C.01, Wallingford, CT.
11. S. F. Boys and F. Bernardi, Molecular physics, 1970, 19, 553-566.
12. R. A. Marcus, Rev. Mod. Phys., 1993, 65, 599-610.
13. V. Coropceanu, J. Cornil, D. A. da Silva Filho, Y. Olivier, R. Silbey and J.-L. Brédas, Chemical Reviews, 2007, 107, 926-952.
14. B.-C. Lin, B. T. Koo, P. Clancy and C.-P. Hsu, The Journal of Physical Chemistry C, 2014, 118, 23605-23613.
15. G. D'Avino, L. Muccioli, Y. Olivier and D. Beljonne, The Journal of Physical Chemistry Letters, 2016, 7, 536-540.
16. T. Wang, X.-K. Chen, A. Ashokan, Z. Zheng, M. K. Ravva and J.-L. Brédas, Advanced Functional Materials, 2018, 28, 1705868.
17. B. Mennucci and J. Tomasi, The Journal of Chemical Physics, 1997, 106, 5151-5158.